Automated Mechanism Generation Using Linear Scaling Relationships and Sensitivity Analyses Applied to Catalytic Partial Oxidation of Methane

Emily J. Mazeau,[*,†] Priyanka Satpute,[†,¶] Katrín Blöndal,[‡]

C. Franklin Goldsmith,[*,‡] and Richard H. West[*,†]

†*Department of Chemical Engineering, Northeastern University, Boston, MA 02115, USA*

‡*School of Engineering, Brown University, Providence, RI 02912, USA*

¶*Current address: Guidehouse, 77 South Bedford St. Suite 400, Burlington, MA 01803, USA*

E-mail: mazeau.e@northeastern.edu; franklin_goldsmith@brown.edu; r.west@northeastern.edu

Phone: +1 (617) 373 5048

Abstract

Kinetic parameters for surface reactions can be predicted using a combination of DFT calculations, scaling relations, and machine learning algorithms; however, construction of microkinetic models still requires a knowledge of all the possible, or at least reasonable, reaction pathways. The recently developed Reaction Mechanism Generator (RMG) for heterogeneous catalysis, now included in RMG version 3.0, is built upon well-established, open-source software that can provide detailed reaction mechanisms from user-supplied initial conditions without making *a priori* assumptions. RMG is now able to estimate adsorbate thermochemistry and construct detailed microkinetic

models on a range of hypothetical metal surfaces using linear scaling relationships. These relationships are a simple, computationally efficient way to estimate adsorption energies by scaling the energy of a calculated surface species on one metal to any other metal. By conducting simulations with sensitivity analyses, users can not only determine the rate limiting step on each surface by plotting a "volcano surface" for the degree of rate control of each reaction as a function of elemental binding energies, but also screen novel catalysts for desirable properties. We investigated the catalytic partial oxidation of methane to demonstrate the utility of this new tool and determined that an inlet gas C/O ratio of 0.8 on a catalyst with carbon and oxygen binding energies of -6.75 eV and -5.0 eV, respectively, yields the highest amount of synthesis gas. Sensitivity analyses show that while the dissociative adsorption of O_2 has the highest degree of rate control, the interactions between individual reactions and reactor conditions are complex, which result in a dynamic rate-limiting step across differing metals.

Keywords

reaction mechanism generation, sensitivity analyses, linear scaling, catalytic partial oxidation, kinetics

Introduction

The modern world is dependent on heterogeneous catalysis, which is essential to important industrial processes in synthesizing high-demand chemicals and materials. There are many catalytic systems of interest which need to be described in great detail, such as upgrading heavy crude oils[1] and converting small molecules like carbon monoxide (CO), carbon dioxide (CO_2), and methane (CH_4) into larger and more valuable compounds such as ethylene or hydrocarbon fuels.[2] Acquiring intimate knowledge of both adsorbed and gas-phase species for one industrially relevant process on a single catalyst is both time consuming and challenging,

motivating the need for a quick and accurate high-throughput prediction and screening method for novel catalysts and reaction conditions.

To develop a molecular level understanding, microkinetic models are constructed considering all possible elementary reactions and intermediate species in the system without *a priori* assumptions of a rate-limiting step or dominant pathway. As these microkinetic models are quite large, complex, and difficult to create by hand, automated model generation is the focus of many researchers; GRACE[3] and KING[4] are the oldest and use a matrix-based representation of species. Some software packages were designed for specific chemistries, such as EXGAS[5] and COMGEN[6] for combustion, PRIM-O[7] and REACTION[8] for heavy molecules, and RING[9] initially for biomass conversion. Others, like RMG,[10,11] Genesys,[12] and KinBot[13] are applicable to a variety of different reactions. KinBot uses on-the-fly Density Functional Theory (DFT) calculations to discover novel reaction pathways and determine accurate thermo-kinetic parameters, but doing so is much slower than applying rules and estimates. Many of these mechanism generation tools are reviewed in ref. 14; very few of them can model heterogeneous catalysis and surface reactions.

Reaction Mechanism Generator (RMG)[10,11] is an open-source software that has been widely used to generate detailed kinetic models for combustion.[15–19] It has recently been extended to heterogeneous catalysis.[20] The current work adds linear scaling relationships to the software.

RMG uses a graph-based approach to represent gas-phase and surface species, with atoms as nodes and bonds as edges. Thermodynamic properties are either obtained from a built-in database or are estimated using group additivity, machine learning, or statistical thermodynamics. Chemical reactions are sorted into predefined families containing reaction templates and recipes to convert chemical graphs from reactants to products. Reaction rates are obtained from a kinetics database or estimated using the Bell-Evans-Polanyi (BEP) principle,[21–26] Equation (1). This states that the difference in activation energy between two similar reactions of the same family is proportional to the difference in the enthalpies of

reaction,

$$E_a = E_a^0 + \alpha \Delta H \qquad 0 \leq \alpha \leq 1 \tag{1}$$

where E_a^0 is determined from the activation energy of a reference reaction, α describes whether the transition state more closely resembles the reactants (closer to 0) or the products (closer to 1), and ΔH is the enthalpy of reaction. The parameters E_a^0 and α, and pre-exponential factors A, are estimated using hierarchical decision trees for each reaction family, stored in the RMG database.

The reaction network is expanded using an iterative, flux-based approach in a core-edge model, where critical species and reactions are initially stored in the core and all possible new species that can be formed are stored in the edge. In its simplest form, species are moved from the edge into the core when the rate of formation, R_i, for species i exceeds a user-defined fraction, ϵ, of the characteristic flux of the core, R_{char}, seen in Equation (2).

$$R_{char} = \sqrt{\sum_{j \in \text{core}} R_j^2} \tag{2}$$

The process repeats until the simulations reach a user defined termination point, such as a species' conversion, with no new species being moved into the core:

$$R_i < \epsilon \cdot R_{char} \qquad \forall i \in \text{edge} \tag{3}$$

To build detailed models of heterogeneously catalyzed processes, surface energetics are needed to determine both thermodynamic and kinetic properties. The adsorption energy, the key property that describes the strength of the interaction between molecules and a surface, can be calculated with reasonable accuracy using density functional theory (DFT).[27] Even though a full understanding of some systems, such as ammonia synthesis, CO oxidation, and propane dehydrogenation, has been obtained through DFT calculations on a single metal,[28–30] investigating such systems on a range of metal and alloy catalysts is still much too

computationally expensive. For these systems, a simple, high-throughput way of estimating binding energies is needed to screen catalysts for desirable properties.

Fortunately, linear scaling relationships provide a simple and computationally efficient way to estimate adsorption energies. Descriptor-based analysis using tools such as CatMAP [31] allows parameters in microkinetic models to be related to one or two descriptors of a surface, such as atomic binding energies. Abild-Pedersen et al. [32] have shown the adsorption energies of hydrogen-containing molecules of carbon, oxygen, sulfur, and nitrogen on transition metal surfaces scale linearly with the adsorption energy of the surface-bonded atom. The adsorption energy of a species $A\mathrm{H}_x$ with central atom A (e.g. C, O, S, or N) is shown as:

$$\Delta E_{ads}^{A\mathrm{H}_x} = \gamma(x)\Delta E_{ads}^{A} + \xi \tag{4}$$

where

$$\gamma(x) = (x_{max} - x)/x_{max} \tag{5}$$

is the slope of the linear relationship between $A\mathrm{H}_x$ and A, and x_{max} is the maximum number of hydrogen atoms that can bond to the central adatom, A (e.g. $x_{max} = 4$ for C and $x_{max} = 2$ for O), and ξ is the intercept, fit to adsorption energy data. Equation (4) can be presented in the following way to determine the adsorption energy on metal $M2$ from a reference metal $M1$:

$$\Delta E_{M2}^{A\mathrm{H}_x} = \Delta E_{M1}^{A\mathrm{H}_x} + \gamma(x)(\Delta E_{M2}^{A} - \Delta E_{M1}^{A}), \tag{6}$$

where the adsorption energy, $\Delta E_{M1}^{A\mathrm{H}_x}$, of a species, $A\mathrm{H}_x$, on a reference metal, $M1$, is used to estimate the adsorption energy, $\Delta E_{M2}^{A\mathrm{H}_x}$, of the same species on another metal, $M2$, from the adsorption energies, ΔE^{A}, of atom A on each metal. These relations hold true for not only fully hydrogenated atoms, but also for larger hydrocarbons, alcohols, aldehydes, carboxylic acids, amines, and others on nitride, sulfide, oxide, transition metal, and select

alloy surfaces.[27,33–47]

Typically, models assume the metric of choice (e.g. TOF) is governed by a single reaction for all binding energies and that the structure of the mechanism is static. The implementation of linear scaling in RMG allows for this presumption to be challenged, as each kinetic model is generated independently for each metal surface. This tool will be paramount in the expedient, high-throughput screening of catalysts for any surface-catalyzed chemical system.

In this article, the catalytic partial oxidation of CH_4 is investigated using these new features in RMG. Catalytic partial oxidation (CPOX) is the catalyzed reaction of hydrocarbons with O_2 to produce a hydrogen-rich synthesis gas consisting of H_2 and CO. This reaction is important in industry because H_2 is used for fossil fuel processing and ammonia production, and CO is used for the bulk manufacturing of aldehydes.[48] Catalytic partial oxidation to produce syngas is also useful in fuel cell applications.[49] Because of its abundance in natural gas, CH_4 is a popular feed-stock.

Linear scaling relationships are used to generate a reaction mechanism on Rh(111), scaling from recently calculated thermodynamic properties for adsorbates on Pt(111).[50] Cantera,[51] an open-source tool for simulating chemical kinetics, thermodynamics, and transport processes, is used to evaluate the mechanism by simulating previously published experimental conditions from Horn et al. in reference 52. This process is repeated for 81 surfaces with different binding energies, and a brute-force sensitivity analysis is carried out to map the degree of rate control of each reaction on each metal.

Methods

Thermodynamic parameter estimates

The RMG adsorbate database currently consists of thermodynamic properties of 69 H/C/O/N-containing species computed using DFT for adsorbates on Pt(111).[50] See reference 50 for details of these calculations. The adsorption thermochemistry of these species (relative to

their gas-phase counterparts) are sorted into decision trees (see Supporting Information) enabling RMG to estimate adsorption thermochemistry for any species.[50] The DFT calculations were performed using the BEEF-vdW functional[53] in the Vienna Ab initio Simulation Package (VASP).[54,55] Each adsorbate considered multiple binding sites and the lowest energy structure was selected. The electronic structure properties were converted into partition functions using standard statistical methods[56] where the potential energy surface of the adsorbates was separated into 1D harmonic oscillator potentials for each of the vibrational modes or adsorbate degrees of freedom (except for weakly bound adsorbates, for which the two lowest vibrational modes were replaced with a 2D gas model), and macroscopic thermodynamic properties, e.g. the enthalpy of formation, entropy, and temperature dependent heat capacity, were derived. These are provided in a NASA polynomial form and added into the RMG database.

During mechanism generation, proposed adsorbates will descend down the decision tree to search for a match in the database. If no exact match is found, the closest structure is used in conjunction with the properties of the adsorbate's gas-phase counterpart. More specifically, a precompiled adsorption correction of the closest structure (or a branch average depending on the new adsorbate's location in the tree) is used to estimate the thermodynamic properties of the new adsorbate by adding the properties to the gas-phase thermochemistry. The gas-phase counterpart properties are acquired either from an exact match in the gas-phase database or estimated via Benson group additivity by RMG.[10,57]

Figure 1 shows a process flow diagram of the entire process. Adsorption energies for species on different metals are estimated with linear scaling relationships, Equation (6), using the thermodynamic estimates on Pt(111) as the reference point. Extrapolation from the Pt(111) point is based on a species' bond order to the surface, as mentioned in the introduction and as seen in Equation (5). The changes in binding energies are then used to calculate the surface species' thermodynamic properties, seen below in Equations (7, 8, 9).

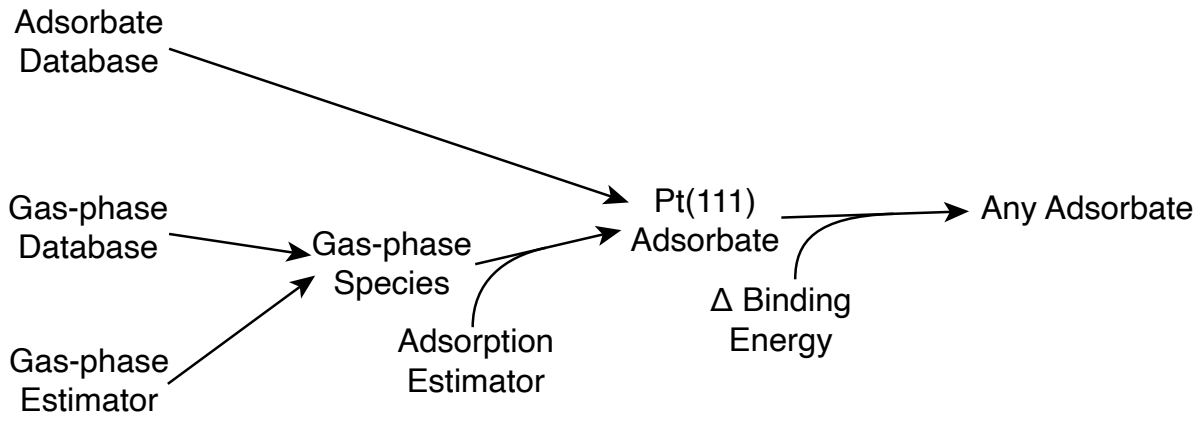

Figure 1: RMG process flowchart for estimating thermodynamic properties.[58]

$$\Delta_f H(298) = \Delta_f H_{gas} + \Delta_{ads} H + \Delta\Delta E_{binding} \tag{7}$$

$$S(298) = S_{gas} + \Delta_{ads} S \tag{8}$$

$$Cp(T) = Cp_{gas} + \Delta_{ads} Cp \tag{9}$$

RMG is currently unable to track multiple distinct adsorption sites; each adsorbate is assumed to always occupy its preferred site, and the scaling correction $\Delta\Delta E_{binding}$ is assumed to scale from the preferred site on the reference metal, Pt(111), to the preferred site on another metal.

Microkinetic model generation and simulations

The kinetic model from Quiceno et al.[59] was included as a library of reactions for RMG to draw from as needed. RMG models were created to be valid at temperatures ranging from 400 K to 2000 K, a pressure of 1 bar, inlet gas stoichiometries with atomic C/O ratios (the ratio of carbon to oxygen atoms in the feed) from 0.6 to 2.6, a surface site density of 2.72×10^{-9} mol/cm^2,[60] a catalyst area per volume of 1.6×10^4 m^{-1},[60] with RMG's

simulation solver tolerances of atol = 10^{-18}, rtol = 10^{-12}, and $\epsilon = 10^{-1}$. 81 models were created independently for surfaces with 9 carbon adsorption energies ranging from −2.0 eV to −7.5 eV and 9 oxygen adsorption energies ranging from −1.5 eV to −6.5 eV. Model generation was halted after the characteristic flux of the system was less than 1% of the maximum characteristic flux reached throughout the model generation, indicating the system had finished reacting.

After building the mechanisms in RMG, models were simulated using Cantera, replicating experiments published by Horn et al. in reference 52, employing a series of 7,000 continuous stirred tank reactors (CSTRs) to act as a plug flow reactor (PFR) (inner diameter = 16.5 mm, length = 70 mm) with porosity = 0.81[60] and the same surface site density and catalyst area per volume used for RMG model generation at atmospheric pressure. The inlet gas flow was held at a constant rate of 4.7 slpm (0.208 mol/min) for 15 different C/O feed gas atomic ratios from C/O = 0.6 to 2.6, where:

$$\mathrm{C/O} = \frac{F_{\mathrm{CH_4}}}{2(F_{\mathrm{O_2}})} \tag{10}$$

$F_{\mathrm{CH_4}}$ is the molar flow rate of CH_4 and $F_{\mathrm{O_2}}$ is the molar flow rate of O_2. The Ar/O_2 ratio was held constant at 79/21. The inlet gas temperature was set to 700 K, the same temperature at the start of the catalyst as seen in experiments published by Horn et al.. The catalyst portion of the PFR was located 10 mm from the inlet and spanned 10 mm, seen in Figure 2.

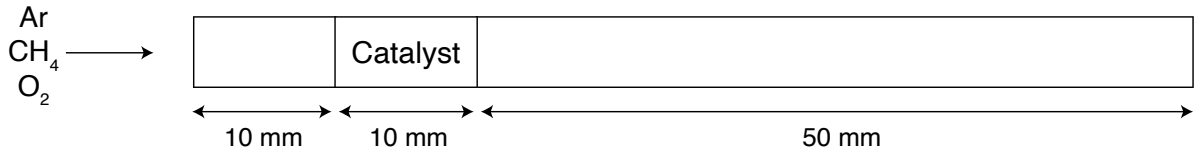

Figure 2: Diagram of the PFR simulated in Cantera and seen in Horn et al..[52]

All surface reactions were 'turned off' for the first 10 mm of the PFR by setting the multipliers to zero, as there are no surface reactions if there is no catalyst. Surface reactions

were turned on by setting multipliers back to 1.0 for 10 mm to 20 mm and back to zero for the remainder of the reactor. Gas-phase reactions remained 'on' for the entirety of the PFR.

From each simulation, the: moles of CH_4 converted, Equation (11), moles of O_2 converted, CO and H_2 (synthesis gas) yield and selectivity, CO_2 and H_2O (full oxidation) yield and selectivity, and temperature at the end of the PFR were obtained. The sum of the selectivities of H_2 Equation (12), and CO Equation (13) was used to describe synthesis gas selectivity Equation (14), seen below:

$$C_{\mathrm{CH_4}} = F_{\mathrm{CH_4},in} - F_{\mathrm{CH_4},out} \tag{11}$$

$$S_{\mathrm{H_2}} = \frac{F_{\mathrm{H_2},out} - F_{\mathrm{H_2},in}}{2(C_{\mathrm{CH_4}})} = \frac{F_{\mathrm{H_2},out}}{2(C_{\mathrm{CH_4}})} \tag{12}$$

$$S_{\mathrm{CO}} = \frac{F_{\mathrm{CO},out} - F_{\mathrm{CO},in}}{C_{\mathrm{CH_4}}} = \frac{F_{\mathrm{CO},out}}{C_{\mathrm{CH_4}}} \tag{13}$$

$$S_{syngas} = S_{\mathrm{H_2}} + S_{\mathrm{CO}} \leq 2.0 \tag{14}$$

$$Y_{syngas} = S_{syngas}\left(\frac{C_{\mathrm{CH_4}}}{F_{\mathrm{CH_4},in}}\right) \tag{15}$$

where F_j is the molar flow rate of a species, j, at the beginning or the end of the PFR. Synthesis gas yield, Equation (15), was calculated by multiplying the synthesis gas selectivity, S_{syngas}, by CH_4 conversion. Full oxidation selectivities and yields were calculated in the same way, replacing H_2 with H_2O and CO with CO_2. Distance to 50% CH_4 conversion was simulated in a PFR that was a maximum of 510 mm length.

Reaction sensitivity analysis

In order to determine which reaction would affect the rate of CH_4 oxidation the most, and therefore be the rate limiting step of the overall reaction, "brute force" sensitivity analyses were performed on each metal surface, increasing the rate of each surface reaction by 1%, one at a time. Sensitivity was measured by comparing the perturbed result of interest to the original result of interest (e.g. conversions, yields, and selectivities, maximum rate of CH_4 conversion, and distance to 50% CH_4 conversion), seen in Equation (16):

$$\sigma_j = \left(\frac{X_{\text{perturbed}} - X_{\text{original}}}{X_{\text{original}}}\right)\left(\frac{k_{j,\text{original}}}{k_{j,\text{perturbed}} - k_{j,\text{original}}}\right) \tag{16}$$

where X is the result of interest (e.g. CO yield), σ_j is the sensitivity with respect to the reaction that was perturbed, and j is a surface reaction index. The perturbation of the rate constant, k_j, in this case is 0.01 or 1%.

A positive σ indicates increasing the rate of reaction increases the result of interest and a negative sensitivity indicates increasing the rate decreases the result. If CH_4 conversion through the reactor was less than 1×10^{-8} mol m^{-1}, all CH_4 and O_2 conversions, yields, and selectivities through the PFR were rounded down to 1×10^{-15} mol m^{-1} (approximately 0, to avoid zero division errors), as the overall reaction was negligible. If a reaction was not found in a microkinetic model (because RMG decided it was not important enough to be included) its sensitivity was set to 0.

Due to convergence issues leading to inaccurate sensitivity results, each Cantera simulation was repeated with relative error tolerances, rtol = 10^{-10}, 10^{-11}, and 10^{-12}, and absolute error tolerances, atol = $10^{-16} \ldots 10^{-24}$, for a total of 27 simulations. Simulations which failed, or which gave sensitivity values that were outliers (more than two times the interquartile range from the quartiles) were excluded, and the remaining values were averaged.

Results and discussion

Model validation

Figure 3 shows the RMG generated model on Rh(111), which consists of 38 gas reactions and 40 surface reactions, found in Table 1. The Rh(111) binding energies of C = −6.568 eV and O = −4.601 eV, as well as those of the other metals marked on the volcano surfaces, were taken from Abild-Pedersen et al..[32] A table of adsorption energies for surface species estimated using RMG compared to literature values is in the Supporting Information (Table S3). Published adsorption energy values derived from DFT tend to have range comparable to the uncertainty from the LSR model, with standard deviation of each species being on average 0.41 eV. The estimates obtained by RMG largely fall within the uncertainty bounds of the published values, with the absolute deviation from the mean of the published values being on average 0.28 eV.

Although CO can adsorb in many configurations,[61–63] RMG does not yet have coverage dependence or site specificity and must represent each species using a chemical graph to represent the Lewis structure. Because Pt(111) is used as the reference surface, where CO adsorbs to the top site via the carbon atom, we represent CO with a double bond from the metal to carbon[50] and, because of the high simulation temperatures, the van der Waals adsorption was manually removed from the mechanism. The complete mechanism is provided in the Supporting Information and reference 58. Figure 4 shows the comparison of simulation results with experimental results on rhodium.

The first step of the mechanism is the dissociative adsorption of O_2 onto the surface. Like other works,[59,64] we do not include molecular adsorption of O_2 prior to dissociation. At such high temperatures, only atomic oxygen will exist on the surface.[65,66] This occurs extremely quickly and fills most surface vacancies, leading to high oxygen surface coverages at the start of the catalyst, seen in the Supporting Information. CH_4 adsorbs much slower in comparison, mostly through dissociative adsorption, and immediately undergoes hydrogen dissociation

Table 1: Surface reaction mechanism of CH_4 oxidation on Rh(111).

	Reaction	Pre-exponential factor	Temperature exponent, n	Activation energy (kcal mol^{-1})
Quiceno et al. reactions				
R1	$2Rh(s) + O_2(s) \leftrightharpoons 2O(s)$	$^{e}1.89\times10^{21}$	-0.5	0.0
R2	$2Rh(s) + H_2 \leftrightharpoons 2H(s)$	$^{a}4.60\times10^{-2}$	0.0	0.0
R3	$H(s) + O(s) \leftrightharpoons Rh(s) + OH(s)$	$^{c}1.28\times10^{21}$	0.0	2.677
R4	$2Rh(s) + CH_4 \leftrightharpoons H(s) + CH_3(s)$	$^{a}9.00\times10^{-4}$	0.0	17.208
R5	$Rh(s) + CH_4 + O(s) \leftrightharpoons CH_3(s) + OH(s)$	$^{e}5.00\times10^{18}$	0.7	10.038
R6	$H(s) + CH_2(s) \leftrightharpoons Rh(s) + CH_3(s)$	$^{c}3.09\times10^{22}$	0.0	0.0
R7	$H(s) + CH(s) \leftrightharpoons Rh(s) + CH_2(s)$	$^{c}3.09\times10^{22}$	0.0	0.0
R8	$Rh(s) + CH(s) \leftrightharpoons H(s) + C(s)$	$^{c}3.09\times10^{22}$	0.0	0.0
R9	$H_2 + C(s) \leftrightharpoons CH_2(s)$	$^{a}4.00\times10^{-2}$	0.0	7.098
R10	$Rh(s) + CO \leftrightharpoons CO(s)$	$^{a}8.40\times10^{-1}$	0.0	0.0
R11	$O(s) + C(s) \leftrightharpoons Rh(s) + CO(s)$	$^{c}3.70\times10^{19}$	0.0	0.0
R12	$Rh(s) + CH_4 + OH(s) \leftrightharpoons CH_3(s) + H_2O(s)$	$^{a}1.00$	0.0	2.39
R13	$Rh(s) + H_2O \leftrightharpoons H_2O(s)$	$^{a}7.50\times10^{-1}$	0.0	0.0
R14	$O(s) + H_2O(s) \leftrightharpoons 2OH(s)$	$^{c}1.00\times10^{20}$	0.0	10.301
R15	$H(s) + OH(s) \leftrightharpoons Rh(s) + H_2O(s)$	$^{c}2.04\times10^{21}$	0.0	15.827
R16	$Rh(s) + CO_2 \leftrightharpoons CO_2(s)$	$^{a}5.00\times10^{-3}$	0.0	0.0
R17	$O(s) + CO(s) \leftrightharpoons Rh(s) + CO_2(s)$	$^{c}3.70\times10^{21}$	0.0	28.107
R18	$H(s) + CO_2(s) \leftrightharpoons OH(s) + CO(s)$	$^{c}1.00\times10^{19}$	0.0	2.008
Van der Waals Adsorption reactions				
R19	$Rh(s) + CH_4 \leftrightharpoons CH_4(s)$	$^{d}1.00\times10^{-1}$	0.0	0.0
R20	$Rh(s) + H_2 \leftrightharpoons H_2(s)$	$^{d}1.00\times10^{-1}$	0.0	0.0
Adsorption reactions				
R21	$Rh(s) + H \leftrightharpoons H(s)$	$^{d}1.00\times10^{-1}$	0.0	0.0
R22	$Rh(s) + OH \leftrightharpoons OH(s)$	$^{d}1.00\times10^{-1}$	0.0	0.0
R23	$Rh(s) + CH_3 \leftrightharpoons CH_3(s)$	$^{d}1.00\times10^{-1}$	0.0	0.0
R24	$Rh(s) + HCO \leftrightharpoons CHO(s)$	$^{d}1.00\times10^{-1}$	0.0	0.0
Dissociative adsorption reactions				
R25	$2Rh(s) + H_2O \leftrightharpoons H(s) + OH(s)$	$^{e}2.00\times10^{-2}$	0.0	14.901
R26	$2Rh(s) + C_2H_6 \leftrightharpoons 2CH_3(s)$	$^{e}1.00\times10^{-2}$	0.0	10.0
R27	$2Rh(s) + CH_3OH \leftrightharpoons CH_3(s) + OH(s)$	$^{e}1.00\times10^{-2}$	0.0	10.0
R28	$2Rh(s) + CH_2O \leftrightharpoons H(s) + CHO(s)$	$^{e}2.00\times10^{-2}$	0.0	10.0
R29	$2Rh(s) + CH_3CHO \leftrightharpoons CH_3(s) + CHO(s)$	$^{e}1.00\times10^{-2}$	0.0	10.0
R30	$2Rh(s) + CH_3CH \leftrightharpoons CH(s) + CH_3(s)$	$^{e}1.00\times10^{-2}$	0.0	10.0
Abstraction reactions				
R31	$OH(s) + CH_2(s) \leftrightharpoons O(s) + CH_3(s)$	$^{c}1.39\times10^{21}$	0.101	4.541
R32	$OH(s) + CH(s) \leftrightharpoons O(s) + CH_2(s)$	$^{c}4.40\times10^{22}$	0.101	10.19
R33	$2CH_2(s) \leftrightharpoons CH_3(s) + CH(s)$	$^{c}1.00\times10^{22}$	0.0	9.56
R34	$OH(s) + C(s) \leftrightharpoons O(s) + CH(s)$	$^{c}2.43\times10^{21}$	-0.312	28.418
R35	$CH_3(s) + C(s) \leftrightharpoons CH_2(s) + CH(s)$	$^{c}1.50\times10^{22}$	0.0	9.56
R36	$C(s) + CH_2(s) \leftrightharpoons 2CH(s)$	$^{c}1.00\times10^{22}$	0.0	9.56
R37	$O(s) + CHO(s) \leftrightharpoons OH(s) + CO(s)$	$^{c}5.00\times10^{21}$	0.0	9.56
R38	$CH_2(s) + CHO(s) \leftrightharpoons CH_3(s) + CO(s)$	$^{c}5.00\times10^{21}$	0.0	9.56
R39	$CH(s) + CHO(s) \leftrightharpoons CO(s) + CH_2(s)$	$^{c}5.00\times10^{21}$	0.0	9.56
R40	$C(s) + CHO(s) \leftrightharpoons CO(s) + CH(s)$	$^{c}5.00\times10^{21}$	0.0	9.56
Dissociation reactions				
R41	$Rh(s) + CHO(s) \leftrightharpoons H(s) + CO(s)$	$^{c}3.71\times10^{21}$	0.0	0.0

^{a} Sticking coefficient (dimensionless); ^{b}pre-exponential factor for unimolecular reactions (s^{-1}); ^{c} pre-exponential factor for bimolecular surface reactions (cm^2 mol^{-1} s^{-1}); ^{d} pre-exponential factor for bimolecular surface and gas reactions (cm^3 mol^{-1} s^{-1}); ^{e}pre-exponential factor for trimolecular reactions (cm^5 mol^{-2} s^{-1})

until fully dehydrogenated. From there, C(s) can combine with oxygen and either desorb partially oxidized, or combine with additional oxygen and desorb fully oxidized. The influx of hydrogens on the surface from CH_4 adsorption can either associatively desorb as H_2, a partial oxidation product, or combine with surface-bound oxygens to create H_2O, a full

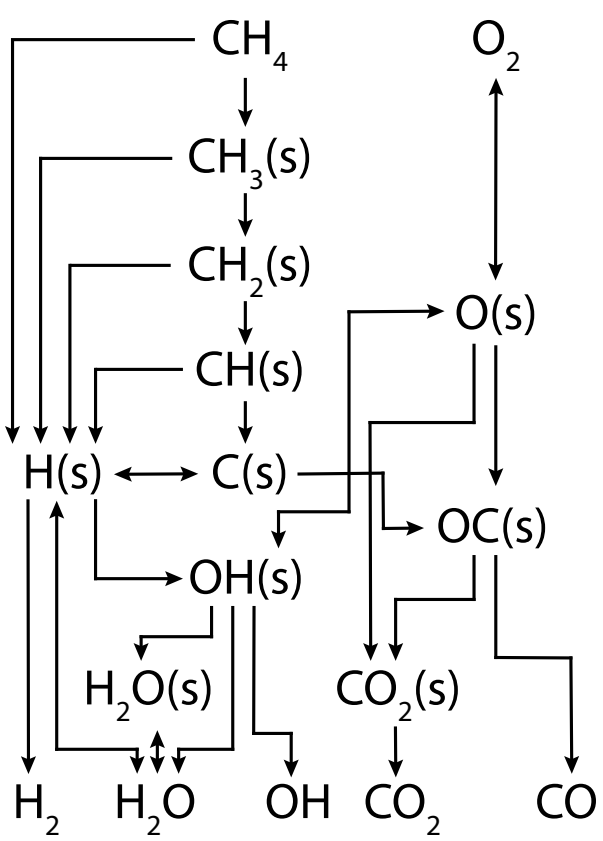

Figure 3: Overall reaction mechanism pathways for Rh(111). Note that not all reactions are shown.[58]

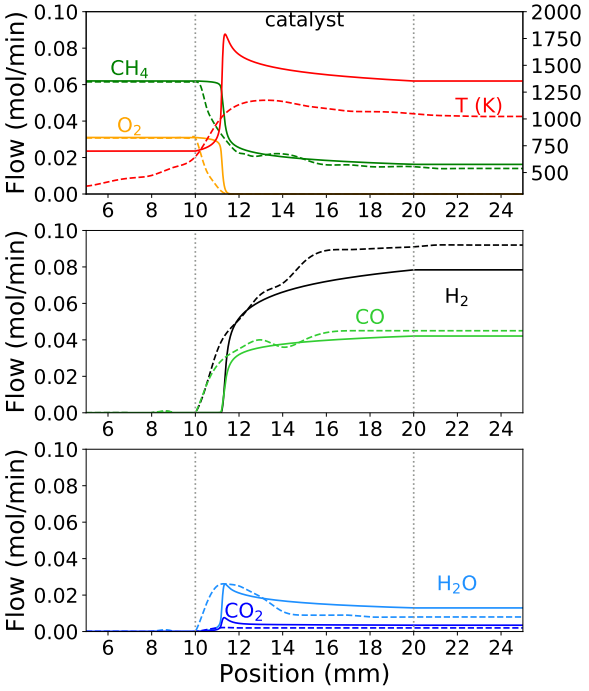

Figure 4: Species and temperature profiles on Rh(111) for inlet gas stoichiometry C/O = 1.0 with Ar as a filler gas at 1 bar from experiments by Horn et al. (dashed lines) and simulations from this work (solid lines). Gases are in contact with the catalyst between the dotted lines.[58]

oxidation product.

Full and partial oxidation zones at C/O = 1.0 are easily identifiable between 11 mm to 11.5 mm along the PFR, seen in the Supporting Information. Full oxidation occurs first, when oxygen is at its highest surface coverage, and as oxygen desorbs, partial oxidation becomes the dominant pathway. Horn et al. identifies the oxidation zone spanning from the catalyst entrance (at 10 mm) to 11 mm, and a steam reforming zone from 11 mm to 19.5 mm. This work finds not only that the oxidation zone occurs in half the distance as experiments, but also a delay in the overall reaction at the start of the catalyst.

There is good agreement for species profiles between the Horn et al. C/O = 1.0 experiments and model simulations, as shown in Figure 4, with H_2 generation roughly 1.75 times more than CO generation. The production of water peaks around the same position as ex-

periments, but there is less H_2O conversion to additional synthesis gas products, as seen in the steam reforming zone that is mentioned in ref. 52. The RMG model had difficulties with predicting the amount of steam reformation, in this case underestimating the amount of H_2 produced, but was able to accurately predict the maximum amount of H_2O.

Most previously mentioned inconsistencies between simulations and experiments can be attributed to the simulation's temperature profile, the most glaring discrepancy, as this system is strongly affected by temperature. Temperature discrepancies can be explained due to the simplicity of the simulated PFR compared to the experimental system because the PFR model was unable to take into account diffusion or convection, causing the observed narrow spike in temperature. There is not only heat conduction through the foam, but also heat conduction through the quartz wall; while the reactor is well insulated, the quartz is thick enough to heat up and redistribute some thermal energy. Horn et al. see the temperature begin to rise much before the catalyst (before the reaction starts), which also proves that there is heat transfer the current reactor model is unable to account for.

At such high temperatures, there will most certainly be mass transport limitations.[67,68] Including mass transport limitations in the model will possibly lead to more gradual rates of disappearance in the oxidation zone, more closely resembling experimental profiles. Another probable cause of error is due to using adsorbate thermodynamics calculated at low coverages. As high surface coverages were observed, species' adsorption energies will decrease as coverage increases, slowing the rates of adsorption. Additionally, many[69–75] advocate for time-shifting, where simulation profiles are shifted along the time axis to match experimental results. A time shift would help account for the model's lag in the onset of oxidation.

Across the 15 different inlet C/O ratios, shown in Figure 5, both O_2 and CH_4 exit conversion have very good agreement with Horn et al.. CH_4 exit conversion decreases as C/O ratio increases because O_2 is consumed before the CH_4 finishes reacting, as there was always 100% O_2 conversion. Both CO and CO_2 exit selectivities had good agreement across all C/O ratios, with the highest CO exit selectivity being at C/O = 1.0 and 1.1 in experiments and

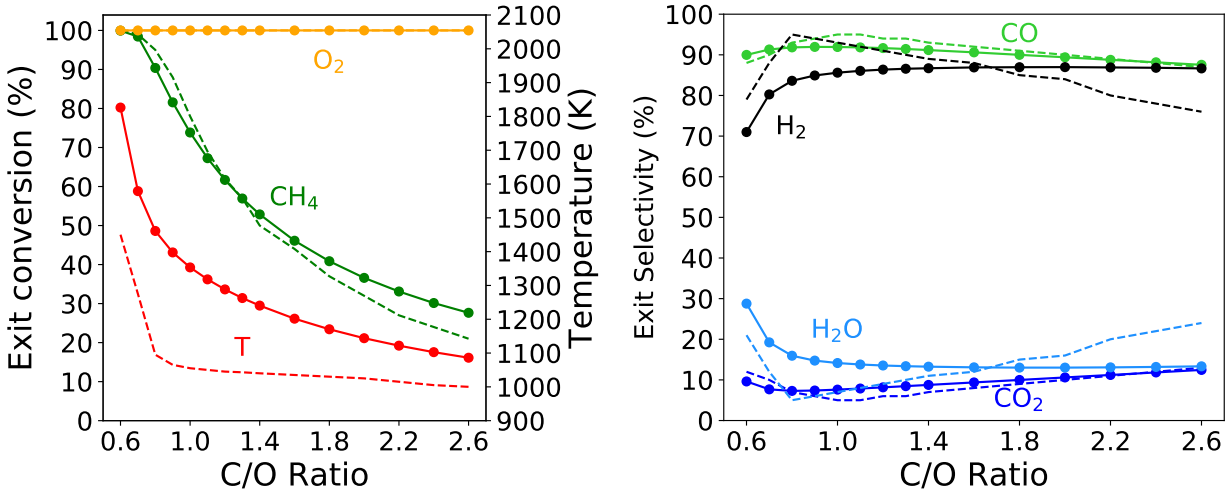

Figure 5: Temperature and conversion (left), selectivities of H_2, CO, H_2O, and CO_2 (right) on Rh(111) at reactor exit at feed C/O = 0.6 - 2.6 and 4.7 slpm. Dotted lines represent experimental data reproduced from Horn et al. and simulations from this work (solid lines).[58]

at C/O = 0.9 in simulations, and lowest CO_2 exit selectivities at C/O = 1.0 and 1.1 in Horn et al. and C/O = 0.8 in this model. Steam reforming selectivity predictions continued to deviate from experimental results, showing some qualitative agreement at low C/O ratios. The model was unable to predict which ratio would have a maximum H_2 exit selectivity (C/O = 0.8 in experiments, C/O = 2.0 in simulations), but did show a slight drop in H_2 exit selectivity after the peak as C/O ratio increases. The trend of overestimating temperature carried over across all C/O ratios, while correctly predicting the qualitative trend.

Regardless of small differences between simulations and experiments, the model automatically generated by RMG using linear scaling corrections, scaled from Pt(111), shows impressive predictive power. This model was generated in under twenty minutes on a single CPU without requiring a single DFT calculation on Rh(111) and was able to effortlessly include both surface and gas-phase chemistry.

Remarkably, this tool was able to generate a mechanism for Rh that shows reasonable quantitative agreement to a complex experiment, which warrants its use to screen and compare different metal surfaces.

Metal catalyst screening

There was little activity on metals with weaker carbon adsorption energies and stronger O_2 adsorption energies (see Supporting Information Figure S5), so a smaller grid spanning carbon adsorption energies from -5.5 eV to -7.5 eV and oxygen adsorption energies from -3.25 eV to -5.25 eV was investigated. This smaller grid allows for a more refined mesh that still encompasses metals of interest, such as Pt and Rh, while trimming away the nonreactive metals.

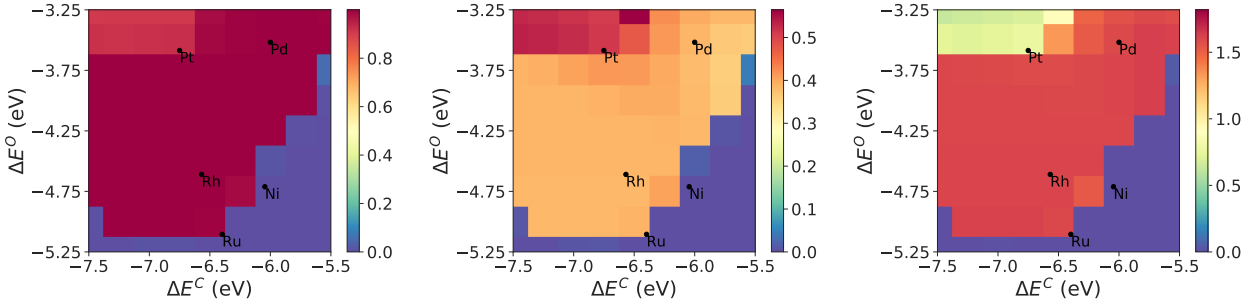

Figure 6: CH_4 conversion (left), full oxidation yield (center), and synthesis gas yield (right) for an inlet gas stoichiometry C/O = 0.6. Note color scales are different.[58]

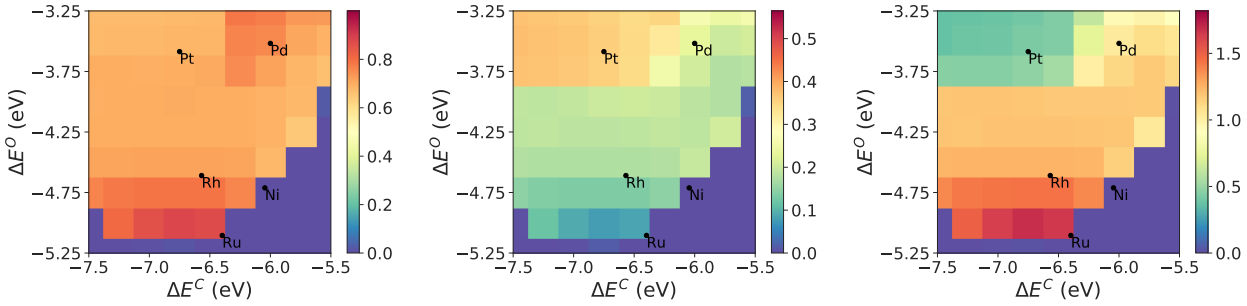

Figure 7: CH_4 conversion (left), full oxidation yield (center), and synthesis gas yield (right) for an inlet gas stoichiometry C/O = 1.0. Note color scales are different.[58]

The volcano surfaces in Figures 6, 7, and 8 show the best metal for synthesis gas yield is a metal with a carbon adsorption energy of $\Delta E^C = -6.75$ eV and an oxygen adsorption energy of $\Delta E^O = -5.0$ eV, which is closest to ruthenium. However, the optimal metal is located close to a steep volcano edge, where slight variations in carbon adsorption energies will cause a rapid decrease in activity. Partial oxidation products are favored as oxygen

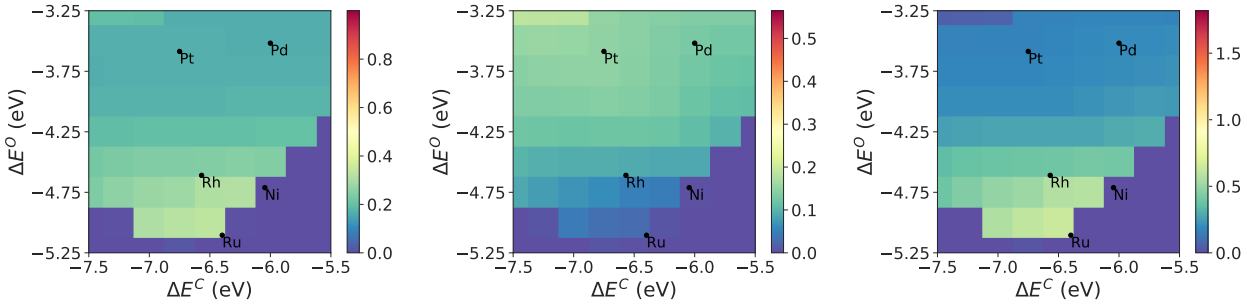

Figure 8: CH_4 conversion (left), full oxidation yield (center), and synthesis gas yield (right) for an inlet gas stoichiometry C/O = 2.6. Note color scales are different.[58]

binds more strongly to the surface, as the adsorption energy of O(s) increases (becomes more negative), making it more difficult for oxygen to leave the surface. There is a plateau, or region with similar activity, at sightly weaker oxygen binding energies. CH_4 conversion follows a similar trend, but with a second high conversion peak occurring on a metal with C adsorption energies in between Pd and Pt, around −6.5 eV, and around an O adsorption energy of −3.5 eV at a C/O ratio = 0.8 to 1.3 (Figure 7). This second 'peak' in conversion is due to the combination of both full and partial oxidation reactions and coincides with an inflection point between metals favoring full oxidation and partial oxidation. Synthesis gas yields decrease as full oxidation yield increases, showing full and partial oxidation pathways are directly in competition with each other.

Comparing Figures 6, 7, and 8 shows that changes in feed stoichiometry do not significantly affect which metal is best (the 'peak' location of the volcano is about the same). Generally, low C/O ratios have higher CH_4 conversion and synthesis gas yields. At higher C/O ratios the selectivity between partial and full oxidation depends more strongly on the metal (Supporting Information Figures S6 and S7). The highest synthesis gas yield was observed at C/O = 0.8 on a metal with $\Delta E^C = -6.75$ eV and $\Delta E^O = -5.0$ eV. This C/O ratio coincides closely with the highest synthesis gas exit selectivities on Rh(111). Sensitivity analyses will show why there are significant drops in yields and conversions that lead to a volcano plot as well as why there is a preference switch between full and partial oxidation as metal properties change.

Reaction sensitivity analyses

Reaction sensitivities on Rh(111) at an inlet gas stoichiometry C/O = 1.0 for CH_4 conversion and synthesis gas yields are seen in the Supporting Information. The most sensitive reaction was R5, the adsorption of CH_4 with an oxygen double bonded to the surface, seen in Table 1.

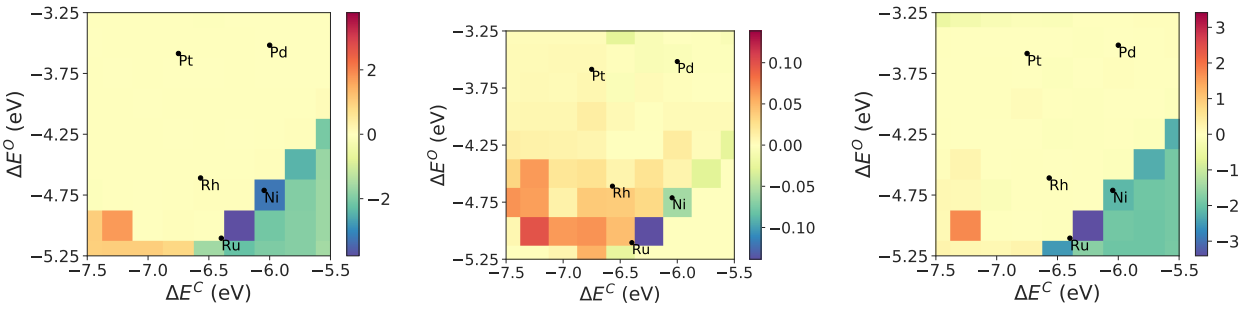

Figure 9: Sensitivity of CH_4 conversion (left), of full oxidation yield (center), and of synthesis gas yield (right) with respect to R1, the dissociative adsorption of O_2, for an inlet gas stoichiometry C/O = 2.4.[58]

Averaging over all inlet gas stoichiometries and metals, the most sensitive reaction was the (reversible) dissociative adsorption of O_2, R1 from Table 1. Figure 9 shows this reaction is mostly sensitive on metals that see low or no CH_4 conversion (*i.e.* on metals with strong oxygen binding energies) suggesting it is one of the main reactions responsible for both the shape and location of the volcano. Speeding up the rate of dissociative adsorption (and associative desorption) slows the entire system (negative sensitivity) on metals with weak carbon and strong oxygen binding energies (bottom right corner), as oxygen will fill empty surface sites before any other species can adsorb, thus blocking the entire reaction from occurring, seen in the Supporting Information. A positive sensitivity indicates O_2 adsorption is the rate limiting step on metals with both strong carbon and oxygen binding energies (bottom left corner). At such strong carbon binding energies, increasing the rate helps adsorb more oxygen to the surface. The rate of dissociative O_2 adsorption is not sensitive on metals that have high CH_4 conversion, and is extremely sensitive when CH_4 conversion decreases (around the 'cliffs' of the volcano plot). CH_4 conversion, full oxidation yield, and partial oxidation yield were all over 30% more sensitive to reaction R1 than to

the next most sensitive reaction.

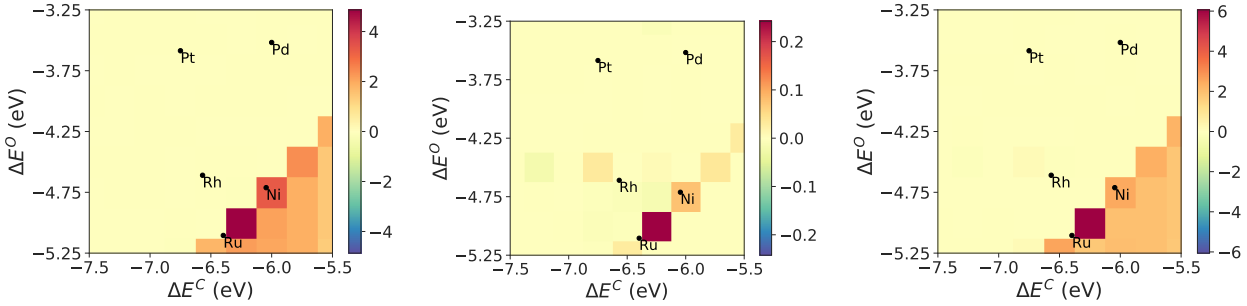

Figure 10: Sensitivity of CH_4 conversion (left), of full oxidation yield (center), and of synthesis gas yield (right) with respect to R6, CH_2 gaining a H from the surface, for an inlet gas stoichiometry C/O = 2.6.[58]

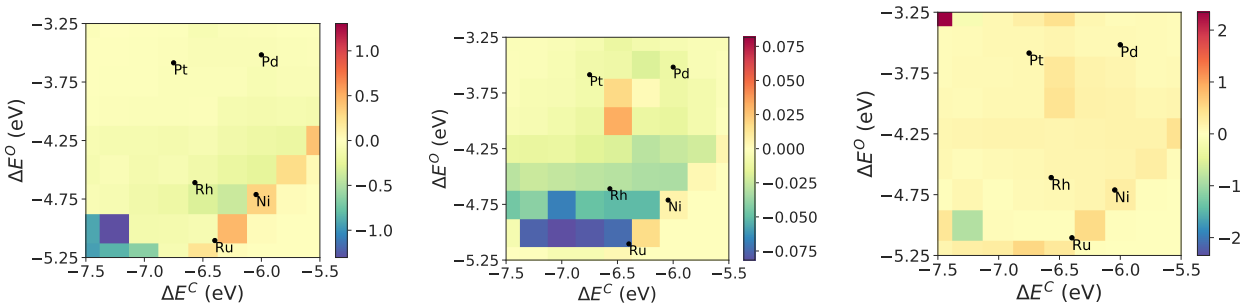

Figure 11: Sensitivity of CH_4 conversion (left), of full oxidation yield (center), and of synthesis gas yield (right) with respect to R5, the adsorption of CH_4 with a surface oxygen, for an inlet gas stoichiometry C/O = 2.4.[58]

R6, hydrogen association to CH_2 as seen in Figure 10, and R5, the dissociative adsorption of CH_4 with a surface oxygen seen in Figure 11, are the next most sensitive reactions and show similar sensitivity. While R6 is slightly more sensitive than R5, both limit methane conversion on metals with weaker carbon binding energies (to the right on the plots).

R5 is one of the first steps in the overall mechanism, and the primary way that CH_4 adsorbs to the surface. Seen in the Supporting Information, R5 increases the selectivity of synthesis gas products and decreases full oxidation products on almost every metal, including metals that have both high and low CH_4 conversions. Full oxidation yield at the 'peak' of the volcano plot has a negative sensitivity, indicating this reaction is responsible for the 'peak' where partial oxidation occurs. R5 also plays a key role in the shape and location

of the volcano, blocking methane conversion on metals with both strong carbon and oxygen binding energies. The other ways for CH_4 to adsorb to the surface, R4 and R12, were over 60% less important in determining CH_4 conversion, full oxidation yield, and partial oxidation yield than R5.

The slight "noise" in Figures 10 and 11 due to numerical imprecision does not change the overall trends, nor the conclusion that there is not a single rate-limiting step. These sensitivity analyses show the rate limiting step changes as both feed ratios and metal change, therefore demonstrating the need for complete microkinetic models.

Caveats and future work

Even though this work moves in a positive direction in the development of low-cost, high-throughput catalyst screening methods, there are some issues that remain with RMG. The first is the model generation, as reaction networks are only expanded if a species or reaction has a high flux relative to the core species. While a reaction or species may have a low initial flux, it may be a precursor to a high flux reaction that should be included in the model. The best way to avoid model truncation errors is to consider all species and reactions regardless of flux, but this significantly increases computational cost and time as well as requires an additional step for model reduction.

The second issue is that RMG does not take into account the effect nearby neighbors have on adsorbate binding energies, which will become more significant in high coverage and high pressure situations. Adding in these coverage dependence corrections will aid in expanding the software's usefulness to industrially relevant conditions, and is planned for future work.

Additionally, RMG does not currently take into account surface geometries or catalyst scaffolds and assumes all surface sites are equivalent, consistent with a Langmuir-Hinshelwood model. In reality, surfaces have multiple types of adsorption sites and each species will have a preferred, lowest energy adsorption site. The introduction of specific surface site types will allow for rate rules specified for the lowest energy site to be used.

While linear scaling is undoubtedly valid for many adsorbates and metals (see data for Rh(111) in Supporting Information Table S3), most models that implement the use of linear scaling are for low adsorbate coverage conditions. These relationships are based on the d-band model,[32] which can predict well for pure metals, but are only valid for a small subset of alloy materials. Xu et al. show that while linear scaling fails for CH_x on AgNi alloys, it is valid for AuNi alloys,[77] meaning changes in adsorption geometries, or adsorbing to specific sites, will affect if linear scaling will be effective. On certain Pt alloys, OOH and OH scale with O_2 but not with O,[78] most likely due to repulsive interactions of an adsorbate with a nearly full electron shell greatly affecting the adsorption energy.[79] In addition to the unreliability of scaling relations, Lee et al. show scaling relations for CH_x combined with BEP relations fails for RhNi alloys while BEP relations with DFT is reliable, revealing problems when combining linear scaling with BEP relations.

With these caveats, the models generated automatically by RMG should be regarded not as a final product, but as a useful starting point for further analysis. A good next step would be performing high level theory DFT calculations on metals in the region identified in the simulations giving highest synthesis gas yield.

Conclusions

Linear scaling relationships[32] have been successfully implemented into RMG to generate unique microkinetic models for any metal surface, scaling from estimates of adsorption on Pt(111), which are based on DFT calculations.[50] RMG models for the catalytic partial oxidation of CH_4 were generated for metal catalysts with carbon adsorption energies ranging from -2.0 eV to -7.5 eV and oxygen adsorption energies from -1.5 eV to -6.5 eV, valid for C/O inlet gas ratios between 0.6 and 2.6 and temperatures from 400 K to 2000 K. Cantera was used to run PFR simulations at 15 C/O inlet ratios, replicated from Horn et al., with brute force sensitivity analyses. CH_4 conversion decreased as C/O inlet gas ratios increased,

showing the effect of running out of O_2. Synthesis gas exit selectivities were greatest for C/O ratios of 0.8 to 1.0, indicating that choking the flow of oxygen does not necessarily ensure partial oxidation selectivity, and there is a 'sweet spot' that fares the best. Despite reactor limitations in Cantera, the model for Rh(111) has good agreement with experimental results, and, more importantly, shows that RMG with linear scaling has predictive power.

PFR simulations were replicated on the same range of novel metals, and showed that full and partial oxidation were in competition with each other at every C/O ratio. The best metal for syngas yield remained roughly the same regardless of C/O ratio. We recommend further study of this region using either higher quality DFT calculations or experiments. There was a clear switch from full oxidation (preferred on metals with weaker O binding energies) to partial oxidation (preferred on metals with stronger O binding energies) on metals with an O adsorption energy between -3.5 eV and -3.75 eV and a more gradual switch from full oxidation (preferred on metals with stronger C binding energies) to partial oxidation (preferred on metals with weak C binding energies) on metals with a C adsorption energy around -6.5 eV. Selectivities for both partial and full oxidation were closer in value at lower C/O ratios and had a larger spread at higher C/O ratios. The ability to estimate both conversion and selectivity as functions of catalyst binding energies, feed composition, reaction conditions, and reactor geometry (eg. residence time), could make predictive tools of this nature very helpful.

Sensitivity analyses showed which reactions are the most sensitive for CH_4 conversion, synthesis gas selectivity and yield, and full oxidation selectivity and yield. The adsorption of O_2 to the surface, R1, is the most sensitive reaction overall, and has both negative and positive sensitivities as metal surface changes. Other reactions control certain regions of the volcano plot, which help to shed light on what causes the volcano plot shape and what controls the location of its peaks and cliffs. R5 is responsible for being negatively sensitive to full oxidation selectivity on metals with high CH_4 conversion (metals of interest).

The sensitivity maps demonstrate the need for microkinetic models formed without *a*

priori assumptions, because the rate limiting step is affected by catalyst properties. Building such models by hand is inefficient, so an open-source tool to do this automatically, for any reaction of interest, is indispensable. RMG can be used to screen novel metal catalysts at a fraction of the cost of experiments and can help elucidate and control complex chemical phenomena that had previously been a mystery.

Acknowledgement

The authors thank Nathan Harms, Sai Krishna Sirumalla, David Medina-Cruz, Chris Blais, David Farina Jr., Nirvana Delgado Otalvaro, and Bjarne Kreitz for helpful suggestions.

This work was supported by the U.S. Department of Energy, Office of Science, Basic Energy Sciences, under Award #0000232253, as part of the Computational Chemical Sciences Program.

The computational work was performed in part using computing resources from the following: National Energy Research Scientific Computing Center (NERSC) operated by Lawrence Berkeley National Laboratory, Discovery cluster supported by Northeastern University's Research Computing team, and Argonne Leadership Computing Facility operated by Argonne National Laboratory.

Supporting Information Available

This information is available free of charge on the ACS Publications website. Additional figures and supporting code can be found in the Supporting Information. In the interests of reproducibility, all data, figures, and scripts are also archived in reference 58.

References

(1) Weissman, J. G.; Kessler, R. V.; Sawicki, R. A.; Belgrave, J. D. M.; Laureshen, C. J.; Mehta, S. A.; Moore, R. G.; Ursenbach, M. G. Down-hole catalytic upgrading of heavy crude oil. *Energy & Fuels* **1996**, *10*, 883–889, DOI: 10.1021/ef9501814.

(2) Lunsford, J. H. Catalytic conversion of methane to more useful chemicals and fuels: a challenge for the 21st century. *Catal. Today* **2000**, *63*, 165–174, DOI: 10.1016/S0920-5861(00)00456-9.

(3) Yoneda, Y. A computer program package for the analysis, creation, and estimation of generalized reactions—GRACE. I. Generation of elementary reaction network in radical reactions—GRACE (I). *Bull. Chem. Soc. Jpn.* **1979**, *52*, 8–14, DOI: 10.1246/bcsj.52.8.

(4) Di Maio, F. P.; Lignola, P. G. KING, a kinetic network generator. *Chem. Eng. Sci.* **1992**, *47*, 2713–2718, DOI: 10.1016/0009-2509(92)87118-A.

(5) Warth, V.; Battin-Leclerc, F.; Fournet, R.; Glaude, P.-A.; Côme, G.-M.; Scacchi, G. Computer based generation of reaction mechanisms for gas-phase oxidation. *Comput. Chem.* **2000**, *24*, 541–560, DOI: 10.1016/s0097-8485(99)00092-3.

(6) Ratkiewicz, A.; Truong, T. N. Application of chemical graph theory for automated mechanism generation. *J. Chem. Inf. Comput. Sci.* **2003**, *43*, 36–44, DOI: 10.1021/ci020297f.

(7) De Bruycker, R.; Pyl, S. P.; Reyniers, M.-F.; Van Geem, K. M.; Marin, G. B. Microkinetic model for the pyrolysis of methyl esters: From model compound to industrial biodiesel. *AIChE J.* **2015**, *61*, 4309–4322, DOI: 10.1002/aic.14953.

(8) Moréac, G.; Blurock, E. S.; Mauss, F. Automatic generation of a detailed mechanism

for the oxidation of n-decane. *Combust. Sci. Technol.* **2006**, *178*, 2025–2038, DOI: 10.1080/00102200600793262.

(9) Rangarajan, S.; Bhan, A.; Daoutidis, P. Rule-based generation of thermochemical routes to biomass conversion. *Ind. Eng. Chem. Res.* **2010**, *49*, 10459–10470, DOI: 10.1021/ie100546t.

(10) Gao, C. W.; Allen, J. W.; Green, W. H.; West, R. H. Reaction Mechanism Generator: automatic construction of chemical kinetic mechanisms. *Comput. Phys. Commun.* **2016**, *203*, 212–225, DOI: 10.1016/j.cpc.2016.02.013.

(11) Liu, M.; Grinberg Dana, A.; Johnson, M. S.; Goldman, M. J.; Jocher, A.; Mark, P. A.; Grambow, C. A.; Han, K.; Yee, N. W.; Mazeau, E. J.; Blondal, K.; West, R. H.; Goldsmith, C. F.; Green, W. H. Reaction Mechanism Generator v3.0: Advances in Automatic Mechanism Generation. *ChemRxiv. Preprint.* **2020**, DOI: 10.26434/chemrxiv.13489656.

(12) Vandewiele, N. M.; Van Geem, K. M.; Reyniers, M.-F.; Marin, G. B. Genesys: Kinetic model construction using chemo-informatics. *Chem. Eng. J.* **2012**, *207*, 526–538, DOI: 10.1016/j.cej.2012.07.014.

(13) Van de Vijver, R.; Zádor, J. KinBot: Automated stationary point search on potential energy surfaces. *Comput. Phys. Commun.* **2020**, *248*, 106947, DOI: 10.1016/j.cpc.2019.106947.

(14) Van de Vijver, R.; Vandewiele, N. M.; Bhoorasingh, P. L.; Slakman, B. L.; Khanshan, F. S.; Carstensen, H. H.; Reyniers, M. F.; Marin, G. B.; West, R. H.; Van Geem, K. M. Automatic Mechanism and Kinetic Model Generation for Gas- and Solution-Phase Processes: A Perspective on Best Practices, Recent Advances, and Future Challenges. *Int. J. Chem. Kinet.* **2015**, *47*, 199–231, DOI: 10.1002/kin.20902.

(15) Keçeli, M.; Elliott, S. N.; Li, Y.-P.; Johnson, M. S.; Cavallotti, C.; Georgievskii, Y.; Green, W. H.; Pelucchi, M.; Wozniak, J. M.; Jasper, A. W.; Klippenstein, S. J. Automated computational thermochemistry for butane oxidation: A prelude to predictive automated combustion kinetics. *Proc. Combust. Inst.* **2019**, *37*, 363–371, DOI: 10.1016/j.proci.2018.07.113.

(16) De Bruycker, R.; Tran, L.-S.; Carstensen, H.-H.; Glaude, P.-A.; Monge, F.; Alzueta, M. U.; Battin-Leclerc, F.; Van Geem, K. M. Experimental and modeling study of the pyrolysis and combustion of 2-methyl-tetrahydrofuran. *Combust. Flame* **2017**, *176*, 409–428, DOI: 10.1016/j.combustflame.2016.11.017.

(17) Chen, X.; Goldsmith, C. F. A Theoretical and Computational Analysis of the Methyl-Vinyl + O_2 Reaction and Its Effects on Propene Combustion. *J. Phys. Chem. A* **2017**, *121*, 9173–9184, DOI: 10.1021/acs.jpca.7b07594.

(18) Chu, T.-C.; Buras, Z. J.; Oßwald, P.; Liu, M.; Goldman, M. J.; Green, W. H. Modeling of aromatics formation in fuel-rich methane oxy-combustion with an automatically generated pressure-dependent mechanism. *Phys. Chem. Chem. Phys.* **2019**, *21*, 813–832, DOI: 10.1039/C8CP06097E.

(19) Goldsborough, S. S.; Fridlyand, A.; West, R.; McNenly, M.; Mehl, M.; Pitz, W. J. *Quantifying Uncertainty in Predictions of Kinetically Modulated Combustion: Application to HCCI Using a Detailed Transportation Fuel Model*; 2018; DOI: 10.4271/2018-01-1251.

(20) Goldsmith, C. F.; West, R. H. Automatic Generation of Microkinetic Mechanisms for Heterogeneous Catalysis. *J. Phys. Chem. C* **2017**, *121*, 9970–9981, DOI: 10.1021/acs.jpcc.7b02133.

(21) Bligaard, T.; Norskov, J. K.; Dahl, S.; Matthiesen, J.; Christensen, C. H.; Sehested, J.

The Bronsted-Evans-Polanyi relation and the volcano curve in heterogeneous catalysis. *J. Catal.* **2004**, *224*, 206–217, DOI: 10.1016/j.jcat.2004.02.034.

(22) Wang, S.; Temel, B.; Shen, J.; Jones, G.; Grabow, L. C.; Studt, F.; Bligaard, T.; Abild-Pedersen, F.; Christensen, C. H.; Nørskov, J. K. Universal Brønsted-Evans-Polanyi Relations for C-C, C-O, C-N, N-O, N-N, and O-O Dissociation Reactions. *Catal. Letters* **2011**, *141*, 370–373, DOI: 10.1007/s10562-010-0477-y.

(23) Sutton, J. E.; Vlachos, D. G. A theoretical and computational analysis of linear free energy relations for the estimation of activation energies. *ACS Catal.* **2012**, *2*, 1624–1634, DOI: 10.1021/cs3003269.

(24) Van Santen, R. A.; Neurock, M.; Shetty, S. G. Reactivity theory of transition-metal surfaces: a Brønsted-Evans-Polanyi linear activation energy- free-energy analysis. *Chem. Rev.* **2009**, *110*, 2005–2048, DOI: 10.1021/cr9001808.

(25) Wang, S.; Vorotnikov, V.; Sutton, J. E.; Vlachos, D. G. Brønsted–Evans–Polanyi and transition state scaling relations of furan derivatives on Pd (111) and their relation to those of small molecules. *ACS Catal.* **2014**, *4*, 604–612, DOI: 10.1021/cs400942u.

(26) Cheng, J.; Hu, P.; Ellis, P.; French, S.; Kelly, G.; Lok, C. M. Brønsted- Evans- Polanyi relation of multistep reactions and volcano curve in heterogeneous catalysis. *J. Phys. Chem. C* **2008**, *112*, 1308–1311, DOI: 10.1021/jp711191j.

(27) Jones, G.; Studt, F.; Abild-Pedersen, F.; Nørskov, J. K.; Bligaard, T. Scaling relationships for adsorption energies of C2 hydrocarbons on transition metal surfaces. *Chem. Eng. Sci.* **2011**, *66*, 6318–6323, DOI: 10.1016/j.ces.2011.02.050.

(28) Hellman, A.; Baerends, E. J.; Biczysko, M.; Bligaard, T.; Christensen, C. H.; Clary, D. C.; Dahl, S.; van Harrevelt, R.; Honkala, K.; Jonsson, H.; Kroes, G. J.; Luppi, M.; Manthe, U.; Nørskov, J. K.; Olsen, R. A.; Rossmeisl, J.; Skúlason, E.;

Tautermann, C. S.; Varandas, A. J. C.; Vincent, J. K. Predicting Catalysis: Understanding Ammonia Synthesis from First-Principles Calculations. *J. Phys. Chem. B* **2006**, *110*, 17719–17735, DOI: 10.1021/jp056982h.

(29) Reuter, K.; Scheffler, M. First-principles kinetic Monte Carlo simulations for heterogeneous catalysis: Application to the CO oxidation at RuO_2 (110). *Phys. Rev. B* **2006**, *73*, 45433, DOI: 10.1103/PhysRevB.73.045433.

(30) Yang, M.-L.; Zhu, Y.-A.; Zhou, X.-G.; Sui, Z.-J.; Chen, D. First-principles calculations of propane dehydrogenation over PtSn catalysts. *ACS Catal.* **2012**, *2*, 1247–1258, DOI: 10.1021/cs300031d.

(31) Medford, A. J.; Shi, C.; Hoffmann, M. J.; Lausche, A. C.; Fitzgibbon, S. R.; Bligaard, T.; Nørskov, J. K. CatMAP: a software package for descriptor-based microkinetic mapping of catalytic trends. *Catal. Letters* **2015**, *145*, 794–807, DOI: 10.1007/s10562-015-1495-6.

(32) Abild-Pedersen, F.; Greeley, J.; Studt, F.; Rossmeisl, J.; Munter, T.; Moses, P.; Skúlason, E.; Bligaard, T.; Nørskov, J. K. Scaling Properties of Adsorption Energies for Hydrogen-Containing Molecules on Transition-Metal Surfaces. *Phys. Rev. Lett.* **2007**, *99*, 4–7, DOI: 10.1103/PhysRevLett.99.016105.

(33) Fernández, E. M.; Moses, P. G.; Toftelund, A.; Hansen, H. A.; Martínez, J. I.; Abild-Pedersen, F.; Kleis, J.; Hinnemann, B.; Rossmeisl, J.; Bligaard, T.; Nørskov, J. K. Scaling relationships for adsorption energies on transition metal oxide, sulfide, and nitride surfaces. *Angew. Chemie* **2008**, *120*, 4761–4764, DOI: 10.1002/ange.200705739.

(34) Montemore, M. M.; Medlin, J. W. Scaling relations between adsorption energies for computational screening and design of catalysts. *Catal. Sci. Technol.* **2014**, *4*, 3748–3761, DOI: 10.1039/c4cy00335g.

(35) Montoya, J. H.; Tsai, C.; Vojvodic, A.; Nørskov, J. K. The challenge of electrochemical ammonia synthesis: A new perspective on the role of nitrogen scaling relations. *ChemSusChem* **2015**, *8*, 2180–2186, DOI: 10.1002/cssc.201500322.

(36) Wang, S.; Petzold, V.; Tripkovic, V.; Kleis, J.; Howalt, J. G.; Skulason, E.; Fernandez, E. M.; Hvolbæk, B.; Jones, G.; Toftelund, A.; Others, Universal transition state scaling relations for (de)hydrogenation over transition metals. *Phys. Chem. Chem. Phys.* **2011**, *13*, 20760–20765, DOI: 10.1039/C1CP20547A.

(37) Ulissi, Z. W.; Medford, A. J.; Bligaard, T.; Nørskov, J. K. To address surface reaction network complexity using scaling relations machine learning and DFT calculations. *Nat. Commun.* **2017**, *8*, 14621, DOI: 10.1038/ncomms14621.

(38) Medford, A. J.; Vojvodic, A.; Hummelshøj, J. S.; Voss, J.; Abild-Pedersen, F.; Studt, F.; Bligaard, T.; Nilsson, A.; Nørskov, J. K. From the Sabatier principle to a predictive theory of transition-metal heterogeneous catalysis. *J. Catal.* **2015**, *328*, 36–42, DOI: 10.1016/j.jcat.2014.12.033.

(39) Salciccioli, M.; Chen, Y.; Vlachos, D. G. Density Functional Theory-Derived Group Additivity and Linear Scaling Methods for Prediction of Oxygenate Stability on Metal Catalysts: Adsorption of Open-Ring Alcohol and Polyol Dehydrogenation Intermediates on Pt-Based Metals. *J. Phys. Chem. C* **2010**, *114*, 20155–20166, DOI: 10.1021/jp107836a.

(40) Vorotnikov, V.; Vlachos, D. G. Group Additivity and Modified Linear Scaling Relations for Estimating Surface Thermochemistry on Transition Metal Surfaces: Application to Furanics. *J. Phys. Chem. C* **2015**, *119*, 10417–10426, DOI: 10.1021/acs.jpcc.5b01696.

(41) Studt, F.; Abild-Pedersen, F.; Bligaard, T.; Sørensen, R. Z.; Christensen, C. H.;

Nørskov, J. K. Identification of non-precious metal alloy catalysts for selective hydrogenation of acetylene. *Science* **2008**, *320*, 1320–1322, DOI: 10.1126/science.1156660.

(42) Sutton, J. E.; Vlachos, D. G. Error estimates in semi-empirical estimation methods of surface reactions. *J. Catal.* **2013**, *297*, 202–216, DOI: 10.1016/j.jcat.2012.10.009.

(43) Xing, B.; Pang, X.-Y.; Wang, G.-C. C–H bond activation of methane on clean and oxygen pre-covered metals: A systematic theoretical study. *J. Catal.* **2011**, *282*, 74–82, DOI: 10.1016/j.jcat.2011.05.027.

(44) Vojvodic, A.; Hellman, A.; Ruberto, C.; Lundqvist, B. I. From electronic structure to catalytic activity: A single descriptor for adsorption and reactivity on transition-metal carbides. *Phys. Rev. Lett.* **2009**, *103*, 146103, DOI: 10.1103/PhysRevLett.103.146103.

(45) Howalt, J. G.; Bligaard, T.; Rossmeisl, J.; Vegge, T. DFT based study of transition metal nano-clusters for electrochemical NH_3 production. *Phys. Chem. Chem. Phys.* **2013**, *15*, 7785–7795, DOI: 10.1039/C3CP44641G.

(46) Fu, Q.; Cao, X.; Luo, Y. Identification of the scaling relations for binary noble-metal nanoparticles. *J. Phys. Chem. C* **2013**, *117*, 2849–2854, DOI: 10.1021/jp311104w.

(47) Skulason, E.; Bligaard, T.; Gudmundsdóttir, S.; Studt, F.; Rossmeisl, J.; Abild-Pedersen, F.; Vegge, T.; Jonsson, H.; Nørskov, J. K. A theoretical evaluation of possible transition metal electro-catalysts for N_2 reduction. *Phys. Chem. Chem. Phys.* **2012**, *14*, 1235–1245, DOI: 10.1039/C1CP22271F.

(48) Christensen, T. S.; Primdahl, I. I. Improve syngas production using autothermal reforming. *Hydrocarb. Process.* **1994**, *73*, 39–44, DOI: 10.1021/acs.iecr.9b01464.

(49) Lee, K. B.; Beaver, M. G.; Caram, H. S.; Sircar, S. Reversible chemisorption of car-

bon dioxide: simultaneous production of fuel-cell grade H_2 and compressed CO_2 from synthesis gas. *Adsorption* **2007**, *13*, 385–397, DOI: 10.1007/s10450-007-9018-4.

(50) Blondal, K.; Jelic, J.; Mazeau, E. J.; Studt, F.; West, R. H.; Goldsmith, C. F. Computer-generated kinetics for coupled heterogeneous/homogeneous systems: a case study in catalytic combustion of methane on platinum. *Ind. Eng. Chem. Res.* **2019**, *58*, 17682–17691, DOI: 10.1021/acs.iecr.9b01464.

(51) Goodwin, D. G.; Speth, R. L.; Moffat, H. K.; Weber, B. W. Cantera: An Object-oriented Software Toolkit for Chemical Kinetics, Thermodynamics, and Transport Processes. https://www.cantera.org, 2018.

(52) Horn, R.; Williams, K. A.; Degenstein, N. J.; Bitsch-Larsen, A.; Dalle Nogare, D.; Tupy, S. A.; Schmidt, L. D. Methane catalytic partial oxidation on autothermal Rh and Pt foam catalysts: Oxidation and reforming zones, transport effects, and approach to thermodynamic equilibrium. *J. Catal.* **2007**, *249*, 380–393, DOI: 10.1016/j.jcat.2007.05.011.

(53) Wellendorff, J.; Lundgaard, K. T.; Mogelhoj, A.; Petzold, V.; Landis, D. D.; Norskov, J. K.; Bligaard, T.; Jacobsen, K. W. Density functionals for surface science: Exchange-correlation model development with Bayesian error estimation. *Phys. Rev. B* **2012**, *85*, DOI: 10.1103/PhysRevB.85.235149.

(54) Kresse, G.; Furthmüller, J. Efficient iterative schemes for ab initio total-energy calculations using a plane-wave basis set. *Phys. Rev. B* **1996**, *54*, 11169–11186, DOI: 10.1103/PhysRevB.54.11169.

(55) Kresse, G.; Furthmüller, J. Efficiency of ab-initio total energy calculations for metals and semiconductors using a plane-wave basis set. *Comput. Mater. Sci.* **1996**, *6*, 15–50, DOI: 10.1016/0927-0256(96)00008-0.

(56) Hill, T. L. *An Introduction to Statistical Thermodynamics*; Dover: New York, 1960.

(57) Goldsmith, C. F. Estimating the Thermochemistry of Adsorbates Based Upon Gas-Phase Properties. *Top. Catal.* **2012**, *55*, 366–375, DOI: 10.1007/s11244-012-9805-3.

(58) Mazeau, E.; Satpute, P.; Blondal, K.; Goldsmith, C. F.; West, R. H. Data for Automated Mechanism Generation Using Linear Scaling Relationships and Sensitivity Analyses applied to Catalytic Partial Oxidation of Methane. Zenodo, 2020; https://doi.org/10.5281/zenodo.4023362.

(59) Quiceno, R.; Pérez-Ramírez, J.; Warnatz, J.; Deutschmann, O. Modeling the high-temperature catalytic partial oxidation of methane over platinum gauze: Detailed gas-phase and surface chemistries coupled with 3D flow field simulations. *Appl. Catal. A Gen.* **2006**, *303*, 166–176, DOI: 10.1016/j.apcata.2006.01.041.

(60) Horn, R.; Williams, K. A.; Degenstein, N. J.; Schmidt, L. D. Syngas by catalytic partial oxidation of methane on rhodium: Mechanistic conclusions from spatially resolved measurements and numerical simulations. *J. Catal.* **2006**, *242*, 92–102, DOI: 10.1016/j.jcat.2006.05.008.

(61) Wang, Y.; de Gironcoli, S.; Hush, N. S.; Reimers, J. R. Successful a priori modeling of CO adsorption on Pt (111) using periodic hybrid density functional theory. *J. Am. Chem. Soc.* **2007**, *129*, 10402–10407, DOI: 10.1021/ja0712367.

(62) Wong, Y. T.; Hoffmann, R. Chemisorption of carbon monoxide on three metal surfaces: nickel (111), palladium (111), and platinum (111): a comparative study. *J. Phys. Chem.* **1991**, *95*, 859–867, DOI: 10.1021/j100155a069.

(63) Kalhara Gunasooriya, G. T. K.; Saeys, M. CO adsorption site preference on platinum: charge is the essence. *ACS Catal.* **2018**, *8*, 3770–3774, DOI: 10.1021/acscatal.8b00214.

(64) Maestri, M.; Vlachos, D. G.; Beretta, A.; Forzatti, P.; Groppi, G.; Tronconi, E. Dom-

inant reaction pathways in the catalytic partial oxidation of CH_4 on Rh. *Top. Catal.* **2009**, *52*, 1983, DOI: 10.1007/s11244-009-9374-2.

(65) Campbell, C. T. An XPS study of molecularly chemisorbed oxygen on Ag (111). *Surf. Sci. Lett.* **1986**, *173*, L641–L646, DOI: 10.1016/0167-2584(86)90808-X.

(66) Spruit, M. E. M.; Kleyn, A. W. Dissociative adsorption of O_2 on Ag (111). *Chem. Phys. Lett.* **1989**, *159*, 342–348, DOI: 10.1016/0009-2614(89)87497-4.

(67) Korup, O.; Goldsmith, C. F.; Weinberg, G.; Geske, M.; Kandemir, T.; Schlogl, R.; Horn, R. Catalytic partial oxidation of methane on platinum investigated by spatial reactor profiles, spatially resolved spectroscopy, and microkinetic modeling. *J. Catal.* **2013**, *297*, 1–16, DOI: 10.1016/j.jcat.2012.08.022.

(68) Dalle Nogare, D.; Degenstein, N. J.; Horn, R.; Canu, P.; Schmidt, L. D. Modeling spatially resolved data of methane catalytic partial oxidation on Rh foam catalyst at different inlet compositions and flowrates. *J. Catal.* **2011**, *277*, 134–148, DOI: 10.1016/j.jcat.2010.10.020.

(69) Burke, S. M.; Metcalfe, W.; Herbinet, O.; Battin-Leclerc, F.; Haas, F. M.; Santner, J.; Dryer, F. L.; Curran, H. J. An experimental and modeling study of propene oxidation. Part 1: Speciation measurements in jet-stirred and flow reactors. *Combust. Flame* **2014**, *161*, 2765–2784, DOI: 10.1016/j.combustflame.2014.05.010.

(70) Zhou, C.-W.; Li, Y.; O'Connor, E.; Somers, K. P.; Thion, S.; Keesee, C.; Mathieu, O.; Petersen, E. L.; DeVerter, T. A.; Oehlschlaeger, M. A.; Kukkadapu, G.; Sung, C.-J.; Alrefae, M.; Khaled, F.; Farooq, A.; Dirrenberger, P.; Glaude, P.-A.; Battin-Leclerc, F.; Santner, J.; Ju, Y.; Held, T.; Haas, F. M.; Dryer, F. L.; Curran, H. J. A comprehensive experimental and modeling study of isobutene oxidation. *Combust. Flame* **2016**, *167*, 353–379, DOI: 10.1016/j.combustflame.2016.01.021.

(71) Haas, F. M.; Chaos, M.; Dryer, F. L. Low and intermediate temperature oxidation of ethanol and ethanol–PRF blends: An experimental and modeling study. *Combust. Flame* **2009**, *156*, 2346–2350, DOI: 10.1016/j.combustflame.2009.08.012.

(72) Sun, H.; Yang, S. I.; Jomaas, G.; Law, C. K. High-pressure laminar flame speeds and kinetic modeling of carbon monoxide/hydrogen combustion. *Proc. Combust. Inst.* **2007**, *31*, 439–446, DOI: 10.1016/j.proci.2006.07.193.

(73) Li, J.; Zhao, Z.; Kazakov, A.; Dryer, F. L. An updated comprehensive kinetic model of hydrogen combustion. *Int. J. Chem. Kinet.* **2004**, *36*, 566–575, DOI: 10.1002/kin.20026.

(74) Zsély, I. G.; Zádor, J.; Turányi, T. Uncertainty analysis of updated hydrogen and carbon monoxide oxidation mechanisms. *Proc. Combust. Inst.* **2005**, *30*, 1273–1281, DOI: 10.1016/j.proci.2004.08.172.

(75) Mueller, M. A.; Kim, T. J.; Yetter, R. A.; Dryer, F. L. Flow reactor studies and kinetic modeling of the H_2/O_2 reaction. *Int. J. Chem. Kinet.* **1999**, *31*, 113–125, DOI: 10.1002/(SICI)1097-4601(1999)31:2<113::AID-KIN5>3.0.CO;2-0.

(76) Xu, Y.; Fan, C.; Zhu, Y.-A.; Li, P.; Zhou, X.-G.; Chen, D.; Yuan, W.-K. Effect of Ag on the control of Ni-catalyzed carbon formation: A density functional theory study. *Catal. Today* **2012**, *186*, 54–62, DOI: 10.1016/j.cattod.2011.08.041.

(77) Huang, Y.; Du, J.; Ling, C.; Zhou, T.; Wang, S. Methane dehydrogenation on Au/Ni surface alloys – a first-principles study. *Catal. Sci. Technol.* **2013**, *3*, 1343–1354, DOI: 10.1039/C3CY20802H.

(78) Hyman, M. P.; Medlin, J. W. Effects of electronic structure modifications on the adsorption of oxygen reduction reaction intermediates on model Pt (111)-alloy surfaces. *J. Phys. Chem. C* **2007**, *111*, 17052–17060, DOI: 10.1021/jp075108g.

(79) Xin, H.; Linic, S. Communications: Exceptions to the d-band model of chemisorption on metal surfaces: The dominant role of repulsion between adsorbate states and metal d-states. *J. Chem. Phys.* **2010**, *132*, 221101, DOI: 10.1063/1.3437609.

(80) Lee, K.; Lee, E.; Song, C.; Janik, M. J. Density functional theory study of propane steam reforming on Rh–Ni bimetallic surface: Sulfur tolerance and scaling/Brønsted–Evans–Polanyi relations. *J. Catal.* **2014**, *309*, 248–259, DOI: 10.1016/j.jcat.2013.10.006.

Graphical TOC Entry